

## An Assessment of the Sea Surface Temperature Influence on Surface Wind Stress in Numerical Weather Prediction and Climate Models

ERIC D. MALONEY AND DUDLEY B. CHELTON

*College of Oceanic and Atmospheric Sciences, Oregon State University, Corvallis, Oregon*

(Manuscript received 24 May 2005, in final form 8 September 2005)

### ABSTRACT

The ability of six climate models to capture the observed coupling between SST and surface wind stress in the vicinity of strong midlatitude SST fronts is analyzed. The analysis emphasizes air–sea interactions associated with ocean meanders in the eastward extensions of major western boundary current systems such as the Gulf Stream, Kuroshio, and Agulhas Current. Satellite observations of wind stress from the SeaWinds scatterometer on NASA's Quick Scatterometer and SST from the Advanced Microwave Scanning Radiometer clearly indicate the influence of SST on surface wind stress on scales smaller than about  $30^\circ$  longitude  $\times$   $10^\circ$  latitude. Spatially high-pass-filtered SST and wind stress variations are linearly related, with higher SST associated with higher wind stress. The influence of SST on wind stress is also clearly identifiable in the ECMWF operational forecast model, having a grid resolution of  $0.35^\circ \times 0.35^\circ$  (T511). However, the coupling coefficient between wind stress and SST, as indicated by the slope of the linear least squares fit, is only half as strong as for satellite observations.

The ability to simulate realistic air–sea interactions is present to varying degrees in the coupled climate models examined. The Model for Interdisciplinary Research on Climate 3.2 (MIROC3.2) high-resolution version (HIRES) ( $1.1^\circ \times 1.1^\circ$ , T106) and the NCAR Community Climate System Model 3.0 ( $1.4^\circ \times 1.4^\circ$ , T85) are the highest-resolution models considered and produce the most realistic air–sea coupling associated with midlatitude current systems. Coupling coefficients between SST and wind stress in MIROC3.2\_HIRES and the NCAR model are at least comparable to those in the ECMWF operational model. The spatial scales of midlatitude SST variations and SST-induced wind perturbations in MIROC3.2\_HIRES are comparable to those of satellite observations. The spatial scales of SST variability in the NCAR model are larger than those in the ECMWF model and satellite observations, and hence the spatial scales of SST-induced perturbations in the wind fields are larger.

It is found that the ability of climate models to simulate air–sea interactions degrades with decreasing grid resolution. SST anomalies in the GFDL Climate Model 2.0 (CM2.0) ( $2.0^\circ \times 2.5^\circ$ ), Met Office Third Hadley Centre Coupled Ocean–Atmosphere General Circulation Model (HadCM3) ( $2.5^\circ \times 3.8^\circ$ ), and MIROC3.2 medium-resolution version (MEDRES) ( $2.8^\circ \times 2.8^\circ$ , T42) have larger spatial scales and are more geographically confined than in the higher-resolution models. The GISS Model E20/Russell ( $4.0^\circ \times 5.0^\circ$ ) is unable to resolve the midlatitude ocean eddies that produce prominent air–sea interaction. Notably, MIROC3.2\_MEDRES exhibits much weaker coupling between wind stress and SST than does the higher vertical and horizontal resolution version of the same model. GFDL CM2.0 and Met Office HadCM3 exhibit a linear relationship between SST and wind stress. However, coupling coefficients for the Met Office model are significantly weaker than in the GFDL and higher-resolution models. In addition to model grid resolution (both vertical and horizontal), deficiencies in the parameterization of boundary layer processes may be responsible for some of these differences in air–sea coupling between models and observations.

### 1. Introduction

Simulating the earth's climate system is critically dependent on accurate representation of ocean–atmosphere interaction at the air–sea interface where the effects of the ocean are communicated to the atmosphere. A robust manifestation of this ocean–atmosphere interaction is the strong relationship between

sea surface temperature (SST) and surface wind stress in regions of strong SST gradients. The objective of this study is to investigate this coupling from analyses of the spatially high-pass-filtered global surface wind stress and SST fields generated by six climate models developed for the Intergovernmental Panel on Climate Change (IPCC) Assessment Report 4 (AR4). The adequacies of the model representations of this ocean–atmosphere coupling is assessed by comparing the relationships between the simulated spatially high-pass-filtered SST and wind stress fields with the relationships deduced from several years of satellite measurements.

Midlatitude ocean–atmosphere interactions on the

---

*Corresponding author address:* Eric D. Maloney, College of Oceanic and Atmospheric Sciences, Oregon State University, 104 COAS Admin. Bldg., Corvallis, OR 97331-5503.  
E-mail: maloney@coas.oregonstate.edu

basin scale are characterized by a negative correlation between surface wind speed and sea surface temperature (see Frankignoul 1985 and Kushnir et al. 2002 for reviews). A first-order model for such interactions is one where SST anomalies are of the same scale as the large-scale atmospheric variability (e.g., Namias and Cayan 1981; Wallace and Jiang 1987), and the ocean mixed layer heat content is locally regulated through wind-driven turbulent fluxes of moist static energy and momentum (e.g., Frankignoul 1985; Barsugli and Battisti 1998). Modifications to this model can be made by accounting for factors such as the horizontal fluxes of heat associated with wind-driven ocean currents (e.g., Luksch and von Storch 1992; Junge and Haine 2001), and advection of cold, dry wintertime continental air over the warmer oceans (e.g., Seager et al. 2000). Wind-driven currents become increasingly important for regulating midlatitude SST variability on decadal and longer time scales (Bjerknes 1964; Deser and Blackmon 1993; Nakamura et al. 1997). The degree to which these basin-scale SST anomalies feed back onto the large-scale atmospheric flow is still an open question, and remains an area of active research (see Kushnir et al. 2002 for a review).

The relationship between SST and surface wind stress on small spatial scales in association with strong SST fronts provides a stark contrast to the large-scale relationships described above. A positive correlation between SST and surface wind stress on scales of order 1000 km is consistently observed from satellite observations in regions of strong SST gradients associated with ocean currents (O'Neill et al. 2003; Xie 2004; Chelton et al. 2004; Small et al. 2005a). The midlatitude eastward extensions of major current systems such as the Gulf Stream, Kuroshio, and Agulhas Current are characterized by meanders and other small-scale eddies that are maintained through forcing by bottom topography (e.g., White and McCreary 1976) and baroclinic and barotropic energy conversions (e.g., Holland and Haidvogel 1980; Ikeda 1981). From long-term averages, it is apparent that some current meanders are tied to bottom-topographic features, with substantial intraseasonal and interannual variability about this mean associated with transient features (Mizuno and White 1983; Nonaka and Xie 2003; Boebel et al. 2003). Advective and eddy oceanic heat fluxes associated with these meanders can apparently maintain SST anomalies in the presence of sustained damping by ocean-atmosphere heat fluxes. Air-sea interactions associated with strong SST fronts also occur in the Tropics. For example, tropical instability waves (TIWs) in the cold tongue region of the tropical east Pacific are associated with small-spatial-scale SST anomalies that exhibit promi-

nent air-sea interactions (Legeckis 1977; Qiao and Weisberg 1995; Chelton et al. 2000, 2001; Hashizume et al. 2001), with a positive correlation between wind stress and SST similar to that found with midlatitude current meanders.

The dynamics and thermodynamics of the observed relation between SST and low-level winds associated with strong SST gradients are not completely understood. Lindzen and Nigam (1987) hypothesized that SST anomalies can force sea level pressure (SLP) and surface wind anomalies through hydrostatic adjustment of the boundary layer to the anomalous surface temperature. Their model assumes that the boundary layer top is a surface of constant pressure and height, and that no pressure gradients are imposed from above the boundary layer. Modifications can be made to include a "back pressure" effect, whereby convergence/divergence of mass forced by the anomalous flow changes the boundary layer height, thereby reducing surface pressure anomalies. Hashizume et al. (2002) suggest a modified back pressure effect whereby deeper boundary layers over warm water and higher inversion heights force a net cold anomaly in the upper boundary layer and reduce SLP anomalies. They argue that back pressure diminished SLP anomalies and their influence on surface winds over the TIW region of the east Pacific. Other modeling and observational analyses continue to suggest that SLP variations may be important for forcing the surface flow near strong SST fronts (e.g., Cronin et al. 2003; Small et al. 2003, 2005b).

Another hypothesis is that decreased stability of the atmospheric boundary layer over the warm side of the SST front increases the surface stress through enhanced downward turbulent mixing of momentum (e.g., Sweet et al. 1981; Jury and Walker 1988; Wallace et al. 1989). Conversely, increased stability over colder water decreases the surface stress through decoupling of the surface winds from the flow aloft. This mechanism requires increasing wind speed with height over colder water in the vicinity of the SST front, a behavior confirmed in some observational studies (e.g., Bond 1992; Hashizume et al. 2002), although disputed by others (e.g., Yin and Albrecht 2000). McGauley et al. (2004) and de Szoeke et al. (2005) showed that surface winds and turbulent mixing increased as the low-level flow crossed northward over the east Pacific cold tongue during the 2001 East Pacific Investigation of Climate experiment (Raymond et al. 2004).

Strong wind stress divergences and curls are generated in association with strong SST fronts (e.g., Chelton et al. 2001, 2004; O'Neill et al. 2003, 2005). The persistence and intensity of Ekman upwelling associated with these wind stress curl perturbations likely have a strong

TABLE 1. List of models examined and their atmosphere resolutions.

Model	Atmosphere dynamical core	Grid resolution (lat $\times$ lon)	No. of vertical levels
ECMWF operational forecast model	Spectral	$0.35^\circ \times 0.35^\circ$ (T511)	60
NCAR CCSM3.0	Spectral	$1.4^\circ \times 1.4^\circ$ (T85)	26
GFDL CM2.0	Gridpoint finite difference	$2.0^\circ \times 2.5^\circ$	24
Met Office HadCM3	Gridpoint finite difference	$2.5^\circ \times 3.8^\circ$	19
GISS Model ER	Gridpoint finite difference	$4.0^\circ \times 5.0^\circ$	20
MIROC3.2_HIRES	Spectral	$1.1^\circ \times 1.1^\circ$ (T106)	56
MIROC3.2_MEDRES	Spectral	$2.8^\circ \times 2.8^\circ$ (T42)	20

feedback on the ocean. Neglect of small-scale variability in the wind stress field can result in underestimates of the volume transports of subtropical western boundary currents by more than 20% (Milliff et al. 2004). Wind stress divergence perturbations and changes in atmospheric boundary layer thickness associated with ocean-atmosphere interaction may also have significant, but currently poorly understood, effects on the midlatitude atmosphere. For example, poor initialization of SST and associated ocean eddies in the Gulf Stream region can impact the ability of forecasting models to simulate developing atmospheric baroclinic systems (E. Rogers 2005, personal communication).

In this study, we examine the ability of a subset of climate models of the IPCC AR4 to capture the observed positive correlation between SST and wind stress on small spatial scales. This analysis focuses on air-sea interactions associated with major midlatitude current systems, but does not address the specifics of the forcing mechanism for these air-sea interactions. Section 2 summarizes the climate models and observational datasets used in this intercomparison. Section 3 describes observed air-sea coupling between wind stress and SST near strong fronts using the National Aeronautics and Space Administration (NASA) Quick Scatterometer (QuikSCAT) observations of ocean vector winds and Advanced Microwave Scanning Radiometer (AMSR) observations of SST. Results from the European Centre for Medium-Range Weather Forecasts (ECMWF) operational forecast model are also shown. Section 4 describes the ability of the IPCC AR4 models to represent the observed coupling between wind stress and SST near strong fronts. Conclusions are presented in section 5.

## 2. Description of models and observations

### a. Climate models

We analyze six of the “Climate of the 20th Century” simulations provided for the IPCC AR4 by interna-

tional modeling centers. These simulations were conducted by forcing the coupled climate models with the best available estimates of the evolution of radiative gases and solar irradiance variations over the last century and a half. Because we are only examining a subset of the IPCC AR4 climate models, care should be taken in generalizing the results of this study to all of the IPCC AR4 simulations.

Here we briefly describe the coupled climate models used in this study. Table 1 summarizes for later reference the salient resolution and dynamical core features of the corresponding atmosphere component models.

#### 1) NCAR CCSM3.0

The National Center for Atmospheric Research (NCAR) Community Climate System Model 3.0 (CCSM3.0) is documented at the following Web site: <http://www.cesm.ucar.edu/>. The atmosphere component, Community Atmosphere Model 3, uses a spectral dynamical core with T85 resolution, corresponding approximately to a horizontal grid resolution of  $1.4^\circ$  latitude  $\times$   $1.4^\circ$  longitude. The model has 26 levels in the vertical, with 4 of these levels being at or below 900 hPa. The oceanic component of CCSM3.0 is a modified version of the Parallel Ocean Program (POP), version 1.4.3, model that was developed at Los Alamos National Laboratory and described in Smith and Gent (2002, more information available online at <http://www.cesm.ucar.edu/>). The version of POP used has a zonal resolution of  $1^\circ$  and a variable meridional resolution that becomes finer as the equator is approached, with an equatorial resolution of about  $0.3^\circ$  latitude. The ocean model has 40 vertical levels. Ocean layer thicknesses increase monotonically from near 10 m at the surface to about 250-m depth.

#### 2) GFDL CM2.0

The Geophysical Fluid Dynamics Laboratory (GFDL) Climate Model 2.0 (CM2.0) is documented in Delworth

et al. (2006). The atmosphere component (Atmosphere Model 2.0) uses a gridpoint dynamical core with a horizontal grid resolution of  $2^\circ$  latitude  $\times$   $2.5^\circ$  longitude and 24 levels in the vertical, with 8 of these levels being at or below 900 hPa. The ocean model (Ocean Model 3.0) is a modified version of the Modular Ocean Model, version 4, with a horizontal resolution of  $1^\circ$  latitude  $\times$   $1^\circ$  longitude in midlatitudes. The meridional resolution becomes finer equatorward of  $30^\circ$  and approaches a resolution of  $1/3^\circ$  latitude at the equator. The ocean model has 50 vertical levels. Twenty-two levels reside in the top 220 m of ocean, each having a thickness of 10 m.

### 3) THE MET OFFICE HADCM3

The Met Office Hadley Centre Third Coupled Model (HadCM3) is documented in Gordon et al. (2000). The atmosphere component, Hadley Centre Atmospheric Model, version 3, uses a gridpoint dynamical core with a horizontal grid resolution of  $2.5^\circ$  latitude  $\times$   $3.8^\circ$  longitude and 19 levels in the vertical, with 3 of these levels being at or below 900 hPa. The ocean component of HadCM3 is described in Gordon et al. (2000), and is a modified version of the ocean model developed by Cox (1984). The ocean model has a horizontal resolution of  $1.3^\circ$  latitude  $\times$   $1.3^\circ$  longitude and 20 vertical levels, with the surface layers having relatively higher resolution than those at depth.

### 4) GISS MODEL ER

The Goddard Institute for Space Studies (GISS) Model E20/Russell (ER) is documented in Schmidt et al. (2006). The atmosphere component (Atmosphere Model 2.0) uses a gridpoint dynamical core having horizontal grid resolution of  $4^\circ$  latitude  $\times$   $5^\circ$  longitude and 20 levels in the vertical, with 3 of these levels being at or below 900 hPa. The ocean model (Russell) is a fully dynamic, non-Boussinesq, mass-conserving free surface ocean model that is documented in Russell et al. (1995). The ocean model has horizontal resolution of  $4^\circ$  latitude  $\times$   $5^\circ$  longitude and 13 levels in the vertical.

### 5) MIROC VERSION 3.2

The Center for Climate System Research (CCSR), University of Tokyo; National Institute for Environmental Studies (NIES); and Frontier Research Center for Global Change (FRCGC) Model for Interdisciplinary Research on Climate, version 3.2 (MIROC3.2), is documented in Hasumi and Emori (2004). We analyze both a high-resolution version (MIROC3.2\_HIRES) and a medium-resolution version (MIROC3.2\_MEDRES) of

this model. The atmosphere component, CCSR/NIES/FRCGC Atmosphere General Circulation Model, version 5.7 (Numaguti et al. 1997), uses a spectral core and has a horizontal grid resolution of  $1.1^\circ$  latitude  $\times$   $1.1^\circ$  longitude (T106) and  $2.8^\circ$  latitude  $\times$   $2.8^\circ$  longitude (T42) for the high- and medium-resolution versions, respectively. The high-resolution model has 56 levels in the vertical, with 8 of these levels below 900 hPa. The medium-resolution model has 20 levels in the vertical, with 4 of these levels below 900 hPa.

The ocean general circulation model is the CCSR Ocean Component Model, version 3.4 (Hasumi 2000). The model uses the primitive equations on the sphere where the Boussinesq and hydrostatic approximations are adopted. The MIROC3.2\_HIRES uses an ocean model with horizontal resolution of  $0.2^\circ$  latitude  $\times$   $0.3^\circ$  longitude and 47 vertical levels. The bathymetry (not shown) is much better resolved than in the NCAR model, with the climate model having the next-highest-resolution ocean component to that of MIROC. The MIROC3.2\_MEDRES uses an ocean model with horizontal zonal resolution of  $1.4^\circ$  longitude, and with meridional resolution of  $0.6^\circ$  at latitudes equatorward of  $8^\circ$  and  $1.4^\circ$  at latitudes poleward of  $65^\circ$ . The medium-resolution ocean model has 43 vertical levels.

## b. Observations

### 1) QUIKSCAT OCEAN VECTOR WINDS

The effect of observed SST variability on surface wind stress is analyzed using ocean vector winds from the NASA QuikSCAT satellite. The SeaWinds scatterometer on QuikSCAT retrieves ocean surface wind stress using the backscatter of microwave radiation from multiple azimuth incidence angles (Chelton and Freilich 2005). QuikSCAT winds have been available since August 1999. The resolution of surface wind estimates is approximately 25 km. Scatterometers are fundamentally stress-measuring instruments. Surface wind estimates are provided as the "equivalent neutral stability wind vector," that is, the wind that would produce the observed wind stress if the atmospheric boundary layer were neutrally stratified. Regardless of the atmospheric stability, surface wind stress is therefore obtained from QuikSCAT wind vectors using the bulk formula for surface drag for neutral stability as developed by Large and Pond and modified by Trenberth et al. (1990). For the analysis presented here, the QuikSCAT wind stress magnitudes were averaged in time over the 4-month period of November 2002–February 2003 on a  $0.25^\circ \times 0.25^\circ$  grid. These fields were then smoothed spatially with a  $2^\circ \times 2^\circ$  loess smoother that

has filtering properties similar to those of  $1.2^\circ \times 1.2^\circ$  block averages but with much smaller sidelobes on the filter transfer function (see Fig. 1 of Chelton and Schlax 2003). The wind stress divergence and curl fields were computed in swath, as described by Chelton et al. (2004), and smoothed with a  $2^\circ \times 2^\circ$  loess smoother.

## 2) AMSR SEA SURFACE TEMPERATURES

We use SST fields from the Advanced Microwave Scanning Radiometer (AMSR) aboard the NASA Earth Observing System (EOS) *Aqua* satellite (Chelton and Wentz 2005). *Aqua* was launched in April 2002, and provides a global retrieval of SST that is possible in cloudy and clear-sky conditions. SST retrievals are only corrupted in regions of precipitation. The footprint of the AMSR allows SST retrievals with horizontal resolution of about 50 km.

### c. Operational products

#### 1) ECMWF OPERATIONAL FORECAST MODEL

Ocean surface wind stress from the ECMWF operational forecast model is used to demonstrate the importance of the resolution and accuracy of the model SST boundary condition to surface winds. The ECMWF forecast model uses a spectral core with T511 resolution, corresponding to a grid resolution of approximately  $0.35^\circ$  latitude  $\times$   $0.35^\circ$  longitude. We use the forecast surface stresses from the ECMWF model rather than the analyzed surface wind fields because these were found to be unbiased compared with QuikSCAT wind stresses. In contrast, the ECMWF 10-m wind analyses are biased 5%–10% low compared with both QuikSCAT and buoy winds (Chelton and Freilich 2005), resulting in a 10%–20% underestimate of wind stress.

#### 2) NOAA REAL-TIME GLOBAL SST

The SST boundary condition in the ECMWF operational forecast model was changed from the Reynolds SST analyses (Reynolds and Smith 1994; Reynolds et al. 2002) to the much higher resolution NOAA real-time global (RTG) SST analyses (Thiébaux et al. 2003) on 9 May 2001 (e.g., Chelton and Wentz 2005). Although both products make use of the same mix of ship, buoy, and infrared satellite data to estimate global SST fields, the spatial decorrelation scale in the objective analysis procedure used for the NOAA RTG product is much shorter than that used for the Reynolds product. The NOAA RTG product uses an isotropic decorrela-

tion scale that is inversely proportional to the local strength of the climatological SST gradients, whereas the Reynolds product effectively prescribes a decorrelation scale of 900 km in the zonal direction by 600 km in the meridional direction. The net effect is that the RTG spatial decorrelation scale of  $\sim 100$  km in the regions of strong SST gradients that are of interest here is significantly shorter than that in the Reynolds SST procedure. The higher-resolution RTG SST fields dramatically improved the post-2001 ECMWF wind stress fields in the regions of strong SST fronts that are of interest in this study (Chelton 2005; Chelton and Wentz 2005).

## 3. Air–sea coupling in satellite observations and the ECMWF operational forecast model

### a. QuikSCAT and AMSR SST

The observed spatially high-pass-filtered QuikSCAT wind stress and AMSR SST are shown in Fig. 1a for the 4-month boreal wintertime period from November 2002 to February 2003. (More detailed or high-resolution versions of the figures are available from the corresponding author.) Wind stress is shown in colors, and SST is shown as contours. We applied a loess spatial high-pass filter with half-power points at  $30^\circ$  longitude and  $10^\circ$  latitude to the SST and wind stress fields. The half-power filter cutoff wavenumbers of this filter are analogous to those of  $18^\circ \times 6^\circ$  block averages. It is seen in Fig. 1a that maxima in the spatially high-pass-filtered wind stress magnitudes coincide with regions of anomalously warm SST, and minima coincide with regions of anomalously cold SST. These relationships are particularly apparent in association with the eddy-induced SST features of the Gulf Stream, Kuroshio, and Agulhas Current systems. Because of the  $30^\circ$  zonal high-pass filtering, zonally elongated SST fronts such as the tropical east Pacific cold tongue are not captured in these fields. Likewise, short-time-scale features such as monthly tropical instability waves are attenuated by the 4-month averaging applied to obtain Fig. 1.

The observed small-scale variability in the midlatitude wind stress magnitude and SST fields is more energetic in winter than in summer, as shown by time series of the spatial standard deviations for the Kuroshio and Agulhas regions (Fig. 2). The regions over which these time series are computed are described in the caption. We analyze standard deviations for the extended September 2002–July 2004 period in this analysis. Seasonal contrasts are largest in the Kuroshio region, where wintertime increases in high-pass-filtered

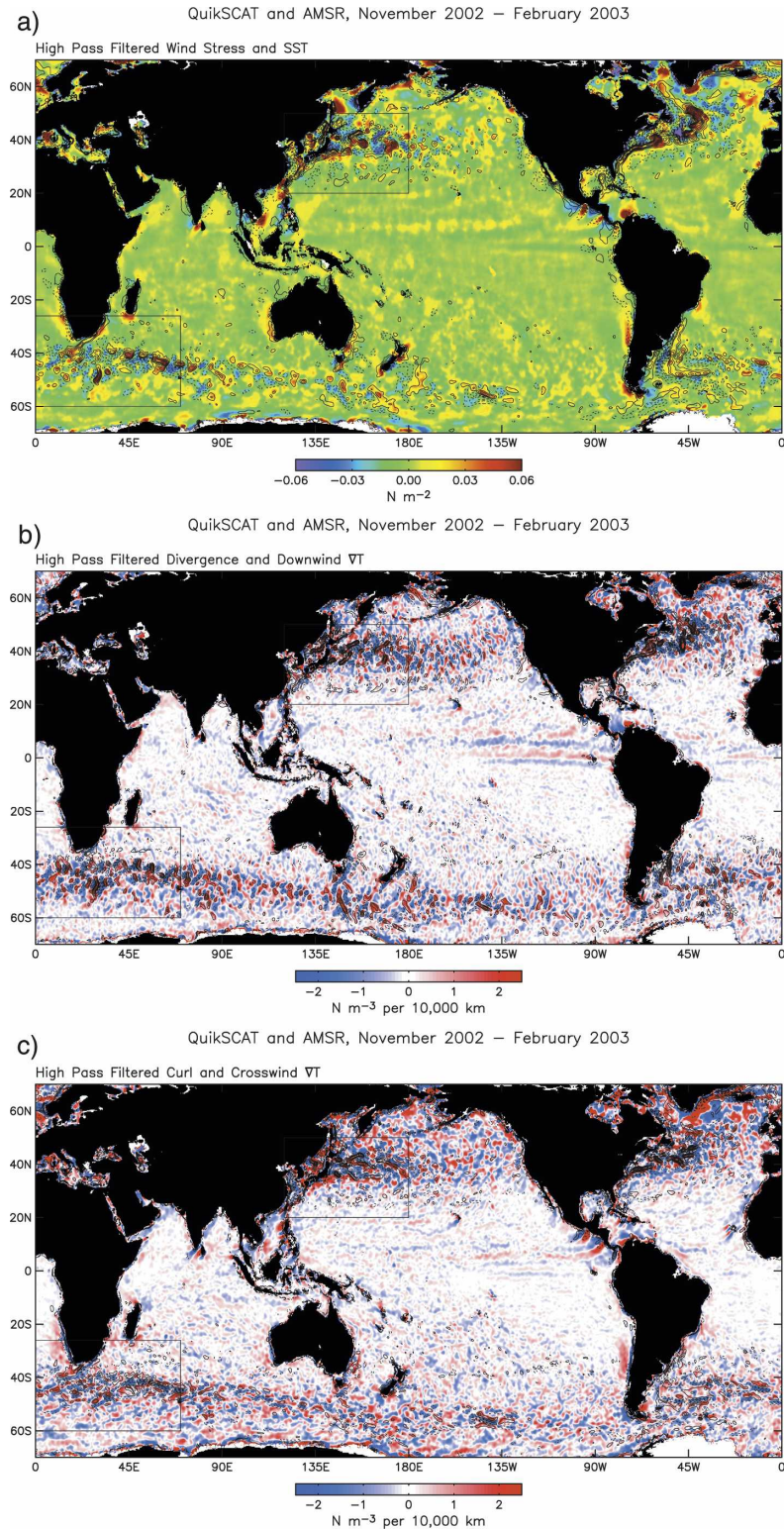


FIG. 1. Spatially high-pass-filtered (a) QuikSCAT wind stress (colors) and AMSR SST (contours), (b) QuikSCAT wind stress divergence (colors) and AMSR downwind SST gradient (contours), and (c) QuikSCAT wind stress curl (colors) and AMSR crosswind SST gradient (contours) averaged over the interval of November 2002–February 2003. The SST contour interval is  $0.5^{\circ}\text{C}$ , with the zero contour omitted. The SST gradient contour interval is  $0.5^{\circ}\text{C} (100\text{ km})^{-1}$ , with the zero contour omitted. A  $10^{\circ}$  latitude  $\times$   $30^{\circ}$  longitude loess spatial high-pass filter was applied to the fields.

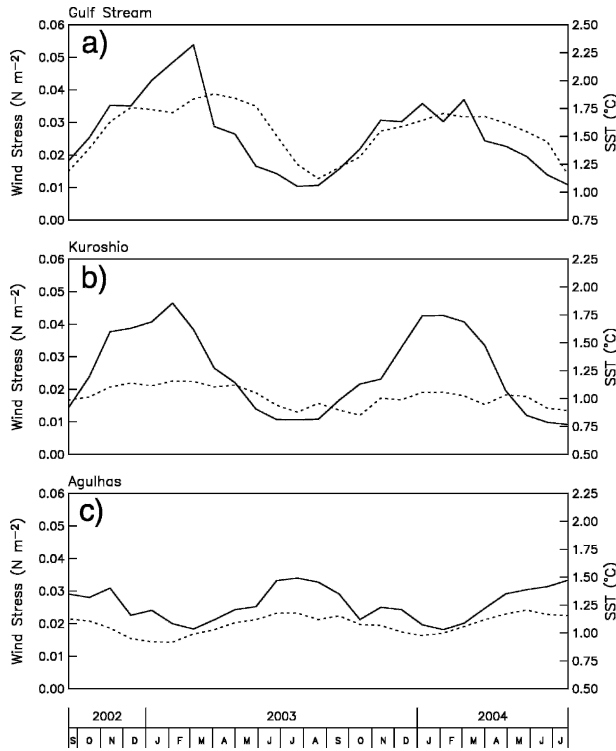


FIG. 2. Time series of the standard deviation of spatially high-pass-filtered QuikSCAT wind stress (solid) and AMSR SST (dashed) for (top) the Gulf Stream region (35°–55°N, 70°–30°W), (middle) the Kuroshio region (32°–50°N, 140°–175°E), and (bottom) Agulhas region (50°–37°S, 10°–90°E). The spatial standard deviations were for 28-day periods from September 2002 to July 2004.

wind stress variability are considerably greater than for SST. This suggests that the stability dependence of the atmospheric boundary layer is important for determining the observed wind stress–SST relationship; larger seasonal changes in mean atmospheric stability from wintertime advection of cold wintertime Asian air over warm water would be expected to force this relatively larger change in wind stress variability over the Kuroshio region. Seasonal contrasts are also large in the Gulf Stream region. Unlike the Kuroshio region, however, there is also large seasonal variability of small-scale perturbations in the SST field in the Gulf Stream region. Seasonal contrasts are comparatively small in both wind stress and the SST field in the Agulhas region.

Because surface wind stress near strong SST fronts is relatively reduced over cold water and enhanced over warm water, prominent wind stress divergence and curl perturbations develop in association with the small-scale features in the SST field. As described in O’Neill et al. (2003) and Chelton et al. (2004), the generation of wind stress divergence and curl depends on the direc-

tion of wind stress relative to the orientation of the SST front. Figure 3 gives a schematic view of how this relationship works for an idealized ocean meander. Divergence (convergence) occurs in association with a downwind (upwind) temperature gradient, and curl occurs in association with a crosswind temperature gradient. As shown in Fig. 3, the crosswind SST gradient is defined as the cross product of the SST gradient with a unit vector in the direction of the wind. The downwind SST gradient is defined as the dot product of the SST gradient with a unit vector in the direction of the wind.

The strong coupling of the derivative wind stress fields to the SST gradient component fields is clearly evident in boreal wintertime global maps. Figure 1b shows high-pass-filtered wind stress divergence with contours of the downwind component of the temperature gradient, and Fig. 1c shows the wind stress curl with contours of the crosswind component of the temperature gradient. Fields are displayed for the same 4-month boreal wintertime period of November 2002–February 2003 shown in Fig. 1a. The spatial covariability is especially high in the Kuroshio and Gulf Stream regions, and in the Southern Ocean where many of the meanders of the Antarctic Circumpolar Current are relatively stationary with respect to the bathymetry.

To quantify the relationship between spatially high-pass wind stress and SST fields, we construct binned scatterplots where we have separated wind stress observations into 0.1°C bins defined by SST perturbation. We define the Kuroshio and Agulhas regions by the boxes in Fig. 1. The left panels in Fig. 4 show the ob-

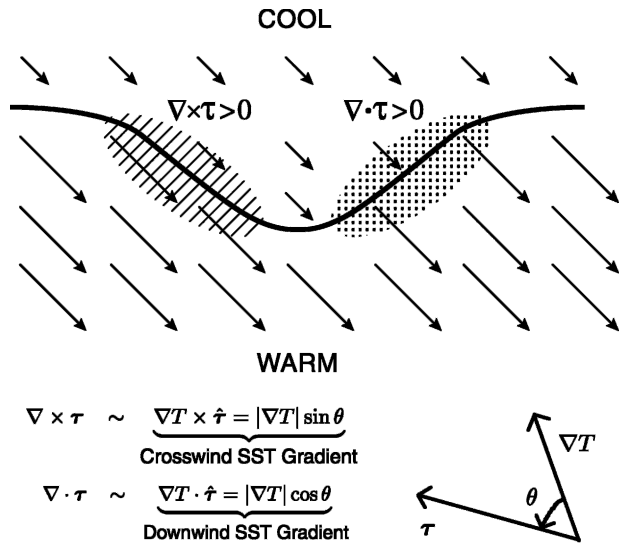


FIG. 3. A schematic representation of how varying SSTs near a strong front influence wind stress, and how these wind stress variations might generate divergences and curls. Vectors of surface wind stress are shown.

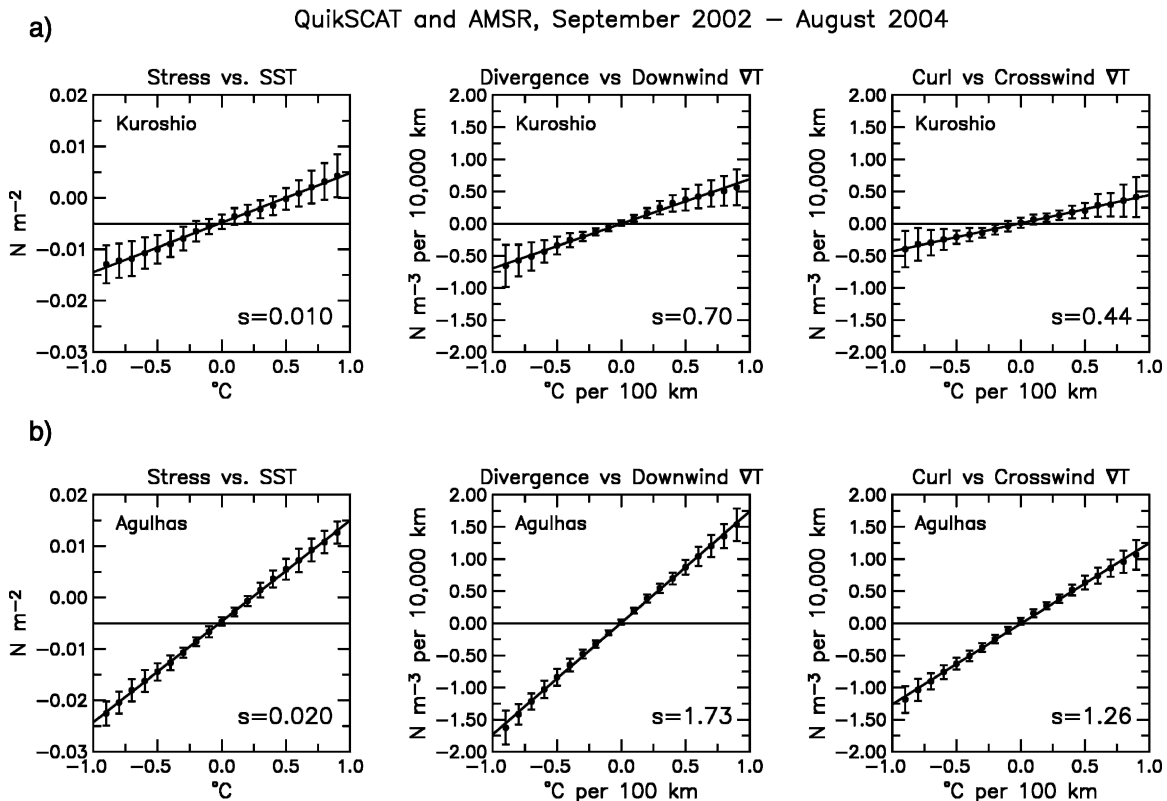


FIG. 4. Binned scatterplots showing spatially high-pass-filtered QuikSCAT wind stress binned by value of AMSR SST perturbation within the (a) Kuroshio and (b) Agulhas regions. Also shown are wind stress divergence vs downwind SST gradient and wind stress curl vs crosswind SST gradient for these same regions. Details of the analysis technique are described in the text.

served relationship between spatially high-pass-filtered SST anomalies and wind stress for the Kuroshio and Agulhas regions, constructed from monthly means over the 2-yr time period of September 2002 through August 2004. Points on the scatterplots show the overall mean value of wind stress anomalies for each SST bin, and error bars denote the  $\pm 1$  standard deviation of the individual binned averages determined from each monthly mean over the 2-yr period. The line through the data represents the linear least squares fit, the slope of which is indicated in the lower-right corner of the panel. The middle and right panels of Fig. 4 show comparable analyses over the same regions for wind stress divergence and the downwind SST gradient, and for wind stress curl and the crosswind SST gradient, respectively.

We use the analysis method described above because the raw point-wise comparisons between high-pass-filtered wind stress and SST show considerable scatter in the monthly means owing to the residual effects of synoptic weather variability. Within each region over which the coupling coefficients are computed, there are areas of small-scale structure in the wind stress outside

of the areas of strong SST gradients because of this synoptic variability. The correlation between wind stress and SST in any particular month is therefore only moderate (typically about 0.5). These effects were mitigated and the relationship between wind stress and SST was isolated by computing the binned average for each individual month over the 2-yr period.

Figure 4 confirms the following strong observed relationships between SST and wind stress in the vicinity of strong SST fronts.

- Wind stress magnitude is linearly related to SST.
- Wind stress divergence is linearly related to the downwind SST gradient.
- Wind stress curl is linearly related the crosswind SST gradient.

These relations are somewhat noisier in the Kuroshio region, due partly to the larger seasonal variability in wind stress that is apparent in Fig. 2, and to the existence of some small-scale variability in the wind field that does not appear to be related to the SST field (e.g., see Fig. 1a). As quantified by the slope of the least

squares fit, the coupling between wind stress and SST is stronger in the Agulhas region ( $0.02 \text{ N m}^{-2} \text{ }^{\circ}\text{C}^{-1}$ ) than in the Kuroshio region ( $0.01 \text{ N m}^{-2} \text{ }^{\circ}\text{C}^{-1}$ ). These different coupling coefficients may be because of the different detailed structure of the atmospheric boundary layer in the two regions, although the greater amount of small-scale wind variability in the Kuroshio region that is independent of SST could also tend to lower the coupling coefficient (regression slope) there.

#### *b. ECMWF operational forecast model*

If we are to expect the relatively coarse resolution-coupled climate models to reproduce the observed relationship between surface wind stress and SST in the vicinity of strong SST fronts, then we would certainly also expect a high-resolution numerical weather prediction model that is forced by a realistic SST boundary condition to reproduce this observed behavior. Here we analyze coupling between SST and wind stress produced by the ECMWF operational forecast model. This model has used a spectral dynamical core with T511 horizontal resolution since November 2000, corresponding to a grid resolution of approximately  $0.35^{\circ}$  latitude  $\times$   $0.35^{\circ}$  longitude. As noted in section 2c, the ECMWF model has used the high-resolution NOAA RTG SST product as a boundary condition since May 2001, in place of the lower-resolution Reynolds SST product that was used previously (Chelton and Wentz 2005). Because of the scarcity of assimilated wind data over open ocean areas, particularly over the Southern Ocean, we would expect the ability of the ECMWF forecast model to reproduce the observed SST-wind stress relationship to be a test of whether model physics respond properly to an imposed SST forcing. Of course, resolution limitations could also affect the model's ability to represent such coupling.

SST influence on low-level winds is clearly represented in the surface wind stress fields from the ECMWF operational forecast model. The spatially high-pass-filtered ECMWF wind stress and NOAA RTG SST are shown in Fig. 5a for the same 4-month boreal winter-time period of November 2002–February 2003 considered in section 3a. Figure 5b shows spatially high-pass-filtered wind stress divergence and contours of the downwind component of the temperature gradient, and Fig. 5c shows the spatially high-pass-filtered wind stress curl and contours of the crosswind component of the temperature gradient. As in satellite observations, wind stress maxima coincide with regions of anomalously warm SST, and wind stress minima coincide with regions of anomalously cold SST. The ECMWF model also exhibits a robust relationship between the down-

wind component of the SST gradient and wind stress divergence, and the crosswind component of the SST gradient and wind stress curl. However, the small-scale SST and wind stress variability is significantly less energetic than in the satellite observations presented in section 3a (see also Fig. 9 below).

Figure 6 shows binned scatterplots from the ECMWF model over the Kuroshio and Agulhas Current regions computed from the 2-yr period September 2002–August 2004. These were calculated in an identical manner to those from satellite observations (Fig. 4). Consistent with the relations obtained from satellite observations,

- ECMWF wind stress magnitude is linearly related to SST.
- ECMWF wind stress divergence is linearly related to the downwind SST gradient.
- ECMWF wind stress curl is linearly related to the crosswind SST gradient.

Compared with the QuikSCAT observations, the coupling coefficients for the ECMWF wind stress field with SST and the SST derivative fields are only about half as large for the wind stress magnitude and wind stress divergence, and only about a third as large for the wind stress curl. The underestimation of the SST influence on low-level winds in the ECMWF model might be because of inadequacies in the parameterization of boundary layer processes, or insufficient vertical resolution in the model. These issues remain ongoing areas of research. We also cannot rule out that the coupling coefficients differ between the ECMWF model and QuikSCAT observations as a result of the ECMWF model being forced by SSTs rather than coupled to a dynamical ocean.

The importance of a realistic SST boundary condition for properly simulating small-scale wind variability in the ECMWF operational model can be clearly demonstrated from comparisons of the ECMWF wind stress before and after the change of the SST boundary condition from Reynolds SST to the higher-resolution NOAA RTG SST analyses on 9 May 2001. Previous studies have demonstrated that this change significantly impacted the spatial resolution of the SST and low-level wind fields in the ECMWF model (Chelton 2005; Chelton and Wentz 2005). Chelton (2005) showed that SST anomalies and air–sea interactions associated with east Pacific tropical instability waves were much better represented in the ECMWF model after the May 2001 implementation of the RTG SST boundary condition. Chelton and Wentz (2005) showed that the higher-resolution RTG SST boundary condition also improved the ECMWF surface wind fields in midlatitude regions.

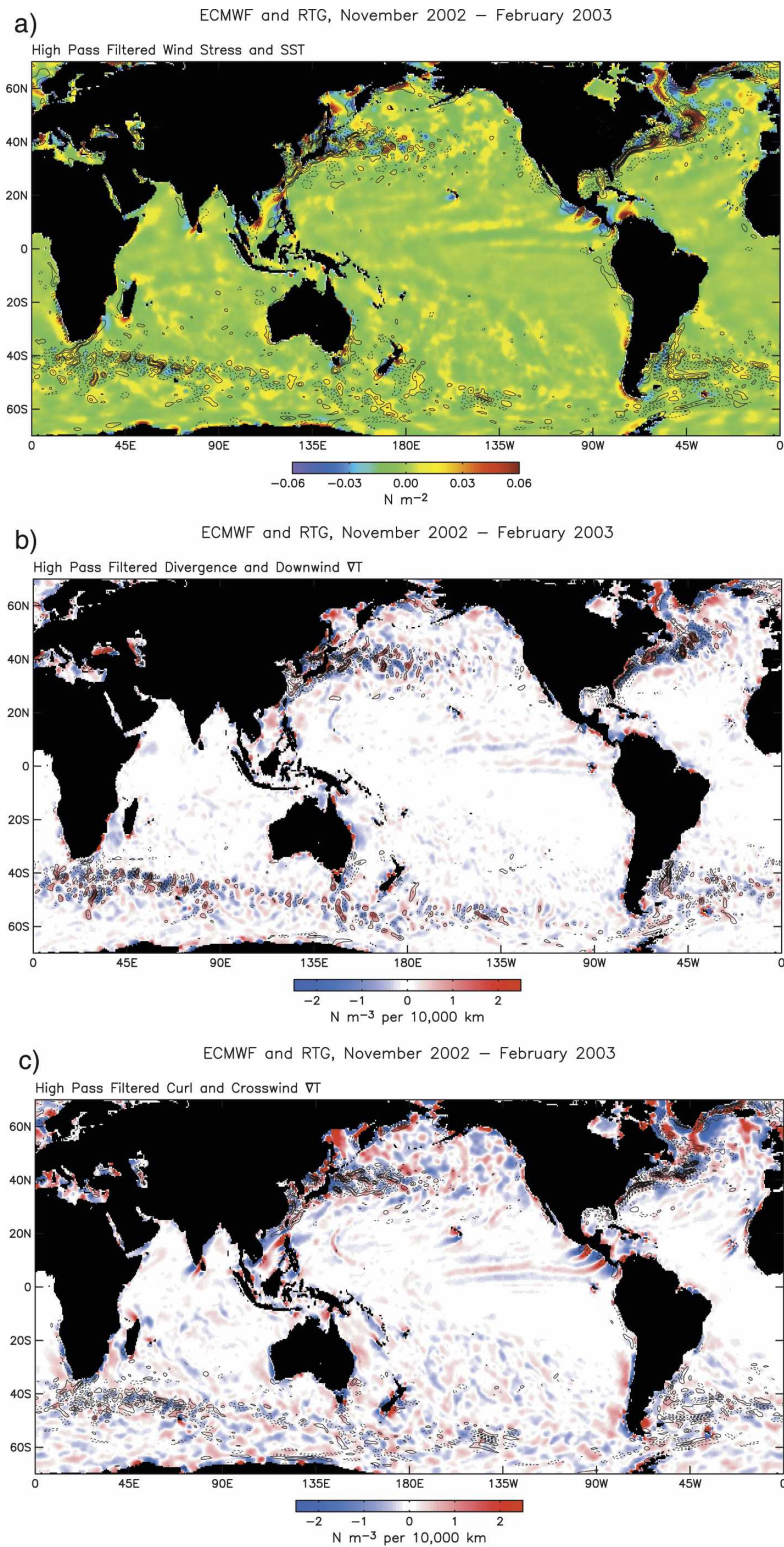


FIG. 5. Spatially high-pass-filtered ECMWF forecasting model (a) wind stress (colors) and NOAA RTG SST (contours), (b) wind stress divergence (colors) and downwind SST gradient (contours), and (c) wind stress curl (colors) and crosswind SST gradient (contours), averaged over the interval of November 2002–February 2003. The SST contour interval is  $0.5^{\circ}\text{C}$ , with the zero contour omitted. The SST gradient contour interval is  $0.5^{\circ}\text{C} (100 \text{ km})^{-1}$ , with the zero contour omitted. A  $10^{\circ}$  latitude  $\times$   $30^{\circ}$  longitude loess spatial high-pass filter was applied to the fields.

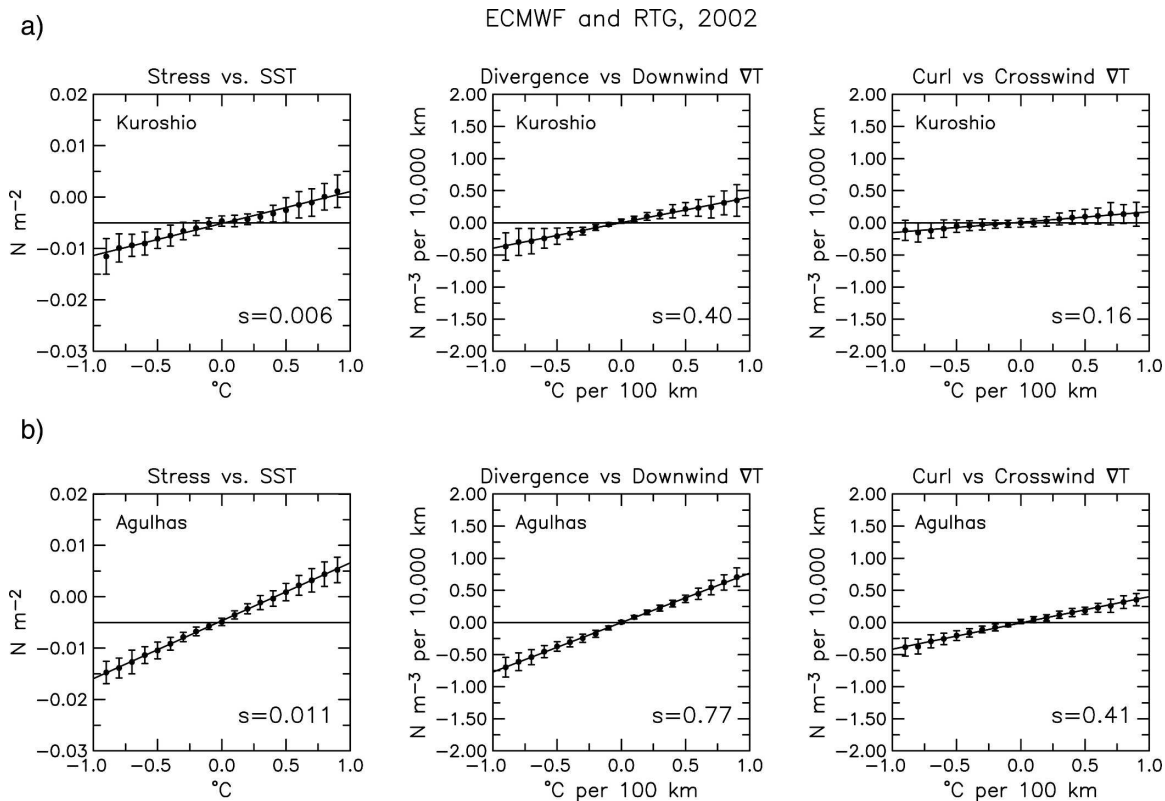


FIG. 6. Same as Fig. 4, but for surface wind stress from the ECMWF operational forecast model and NOAA RTG sea surface temperatures for 2002.

The sensitivity of the ECMWF model to specification of the SST boundary condition is evident from Fig. 7, which shows the small-scale wind stress magnitude and SST fields in the Gulf Stream, Kuroshio, and Agulhas regions averaged over 4 weeks before (left) and after (right) the change in the SST boundary condition of the ECMWF model. High spatial wavenumber SST perturbations are dramatically more energetic after the change in boundary condition, and the corresponding observed modulation of surface wind stress by these SST features is much better captured. Air–sea coupling is climatologically weak during May in the Kuroshio extension region compared with other regions, and so the change in SST boundary condition is not as dramatic there. Air–sea coupling in the Kuroshio region is significantly stronger during other months (not shown here). The heavy spatial and temporal smoothing (900 km zonally  $\times$  600 km meridionally  $\times$  7 days temporally) of the Reynolds SST product is unable to fully resolve meanders in the Gulf Stream, Kuroshio, and Agulhas regions. As a result, the actual SST modulation of the wind stress field is poorly captured.

The results of Fig. 7 have important implications for

coupled climate models. The ability of models to produce realistic air–sea interactions in major ocean currents regions is crucially dependent on the ability of ocean models to resolve the SST features associated with current meanders and other localized dynamical features that create strong SST fronts. All of the climate models considered in section 4 have ocean components with higher grid resolution than their corresponding atmosphere components. Except for the high-resolution MIROC, the midlatitude grid resolutions of the ocean components of all the coupled models considered here are at least a factor of 2 coarser than the resolution of the RTG fields, thus limiting the model representations of the observed SST influence on the surface wind stress.

#### 4. SST–surface wind stress coupling in IPCC AR4 models

The six coupled climate models analyzed here have ocean components with equal or higher grid resolution than the corresponding atmosphere models. The SST influence on surface wind stress is reproduced to vary-

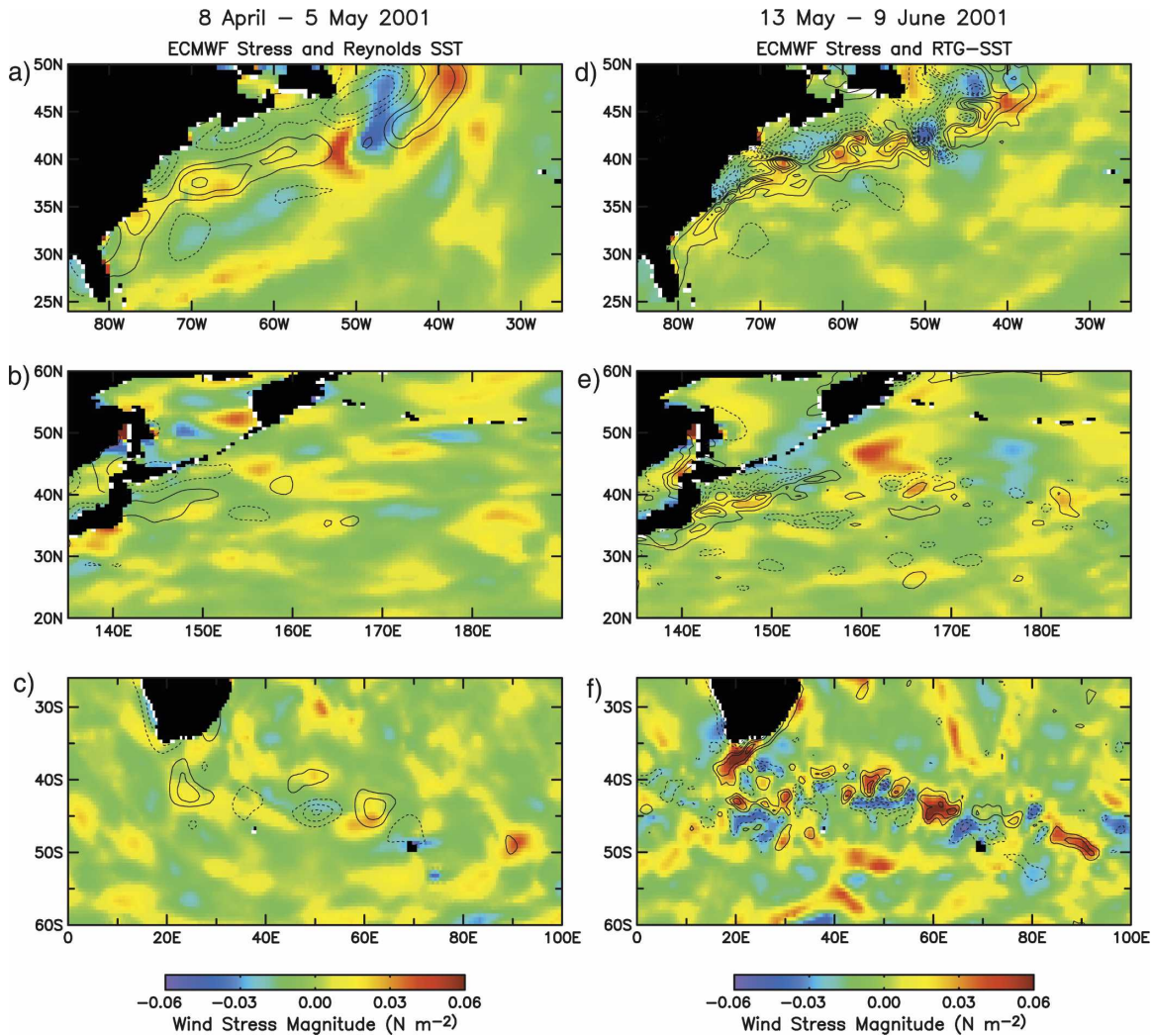


FIG. 7. Spatially high-pass-filtered ECMWF operational forecasting model wind stress (colors) and SST (contours) averaged over the interval of (left) 8 Apr–5 May 2001 prior to the switch to NOAA RTG SST, and (right) 13 May–9 Jun 2001 after the switch to NOAA RTG SST. The Gulf Stream, Kuroshio, and Agulhas regions are shown. Contour interval is  $1.0^{\circ}\text{C}$ , with the zero contour omitted. A  $10^{\circ}$  latitude  $\times$   $30^{\circ}$  longitude loess spatial high-pass filter was applied to the fields.

ing degrees in these six models. Figure 8 shows 4-month-averaged maps (November 1998–February 1999 of each model run) of  $30^{\circ} \times 10^{\circ}$  spatially high-pass-filtered SST (contours) and wind stress (colors). The covariability of SST with wind stress is clearly present in the high-resolution MIROC and NCAR model, and to a lesser extent in the GFDL model and medium-resolution MIROC. However, this covariability, even in the highest-resolution models, is reduced in intensity compared with observations (note the factor-of-2 differences in the dynamic range of the color bars and in the contour intervals compared with Figs. 1a and 5a).

The spatial scales of variability in the climate models

are generally also much larger in the SST and wind stress fields than in either the satellite observations (Fig. 1a) or the ECMWF operational forecast model (Fig. 7). The one notable exception is the high-resolution MIROC. Figure 9 shows zonal wavenumber spectral densities for the SST and wind stress fields in satellite observations, the ECMWF operational forecast model, and the high-resolution MIROC and NCAR climate model. The spatial scales of SST variability in MIROC are comparable to those of satellite observations and the ECMWF forecast model over both the Kuroshio and Agulhas Current regions. The NCAR model underestimates SST variability at the smallest-space scales relative to satellite observations.

The high-resolution MIROC underestimates the shortest-space scales of variability in wind stress (<500 km) that is present in satellite observations (Figs. 9b and 9d).

The Southern Ocean is the region of the greatest zonal extent of small-scale SST variability in the observations (Fig. 1a). Coupled SST and wind stress anomalies exist throughout the Southern Ocean in the high-resolution MIROC and NCAR model, but are less intense and more restricted geographically in the GFDL model and medium-resolution MIROC. The Met Office model has patches of SST variability throughout the Southern Ocean, although covariance with wind stress is not strong and the spatial scales are much too large. The ability of the GISS model to capture Southern Ocean SST variability is limited by the very coarse  $4^\circ \times 5^\circ$  resolution of the model.

Binned scatterplots of spatially high-pass-filtered SST and wind stress for the Kuroshio and Agulhas regions are shown for each coupled climate model to the right of the maps in Fig. 8. The high-resolution MIROC (Fig. 8e) exhibits coupling between SST and wind stress that is comparable to that from the ECMWF operational forecast model (Fig. 6). Notably, SST–wind stress coupling weakens dramatically in the medium-resolution MIROC (Fig. 8f). Because both the horizontal and vertical resolutions are degraded in the medium-resolution MIROC, we cannot separate their relative importance in producing the changes in the coupling coefficient. These results do, however, indicate the importance of resolution, rather than model physics alone, for simulating realistic air–sea interactions in the midlatitude oceans. The high-resolution MIROC represents the atmospheric boundary layer by about twice as many layers as the medium-resolution version of the model. This may account for the more realistic coupling coefficients in this version of the model.

The coupling coefficients for the NCAR and GFDL models are only somewhat weaker than those for the ECMWF operational forecast model (Fig. 6). However, because the SST anomalies are weaker in the NCAR and GFDL models, so are the wind stress anomalies. Patches of covariability of wind stress magnitude and SST can be found in the map for the Met Office model, but regions also exist where SST and wind stress magnitude are negatively correlated. Consequently, no clear relation emerges in the binned scatterplots for the Met Office model. The resolution of the GISS atmospheric model is too coarse to resolve the small-scale features in the SST field that influence the low-level winds.

It is significant that, even in the highest-resolution climate model considered here (the high-resolution

MIROC), the coupling coefficients are only half as large as those inferred from satellite observations (Fig. 4). This is very similar to the underestimate of the wind stress response to SST in the ECMWF operational model (Fig. 6). While both the high-resolution MIROC and ECMWF model provide simulations with exceptionally high spatial resolution, their vertical and horizontal resolution capabilities are still limited and likely contribute to the weaker coupling in wind stress and SST than in satellite observations. The dramatically reduced SST–wind stress coupling in the medium-resolution MIROC is a clear demonstration of the resolution dependence of the coupling. We cannot rule out the possibility that deficiencies in the parameterization of boundary layer processes also contribute to the weaker coupling coefficients in the models than observations. Biases in the large-scale model climate could also influence these coupling coefficients (e.g., errors in the position of the midlatitude atmospheric westerly flow).

The models that are best able to produce the observed coupling between wind stress and SST are also the models that are best able to produce the observed relationship between SST-derivative fields and the wind stress divergence and curl fields. Wind stress curl and the attendant oceanic vertical Ekman velocities are crucial for forcing the wind-driven circulation of the ocean. Model biases in wind stress curl may therefore impact the ability of coupled climate models to simulate the ocean general circulation, as has been noted recently by Milliff et al. (2004). As in the satellite observations and the ECMWF forecast model, prominent covariabilities exist in the high-resolution MIROC and NCAR model between the wind stress divergence and downwind SST gradient (Fig. 10a), and between the wind stress curl and crosswind SST gradient (Fig. 10b). For the other climate models considered here, the coupling between SST gradient components and wind stress divergence and curl become decreasingly robust as the model grid resolution decreases (not shown here).

The visual covariabilities in Fig. 10 are quantified in Fig. 11, which displays binned scatterplots of wind stress divergence versus the downwind temperature gradient, and wind stress curl versus the crosswind SST gradient, from the NCAR model and high-resolution MIROC. As in Figs. 4 and 6, the scatterplots are calculated over the Kuroshio and Agulhas Current regions. While coupling in the NCAR model and MIROC is generally weaker than for satellite-derived SST gradient and wind stress–derivative fields (Fig. 4), the coupling coefficients shown here are comparable to, and sometimes exceed, those from the ECMWF model

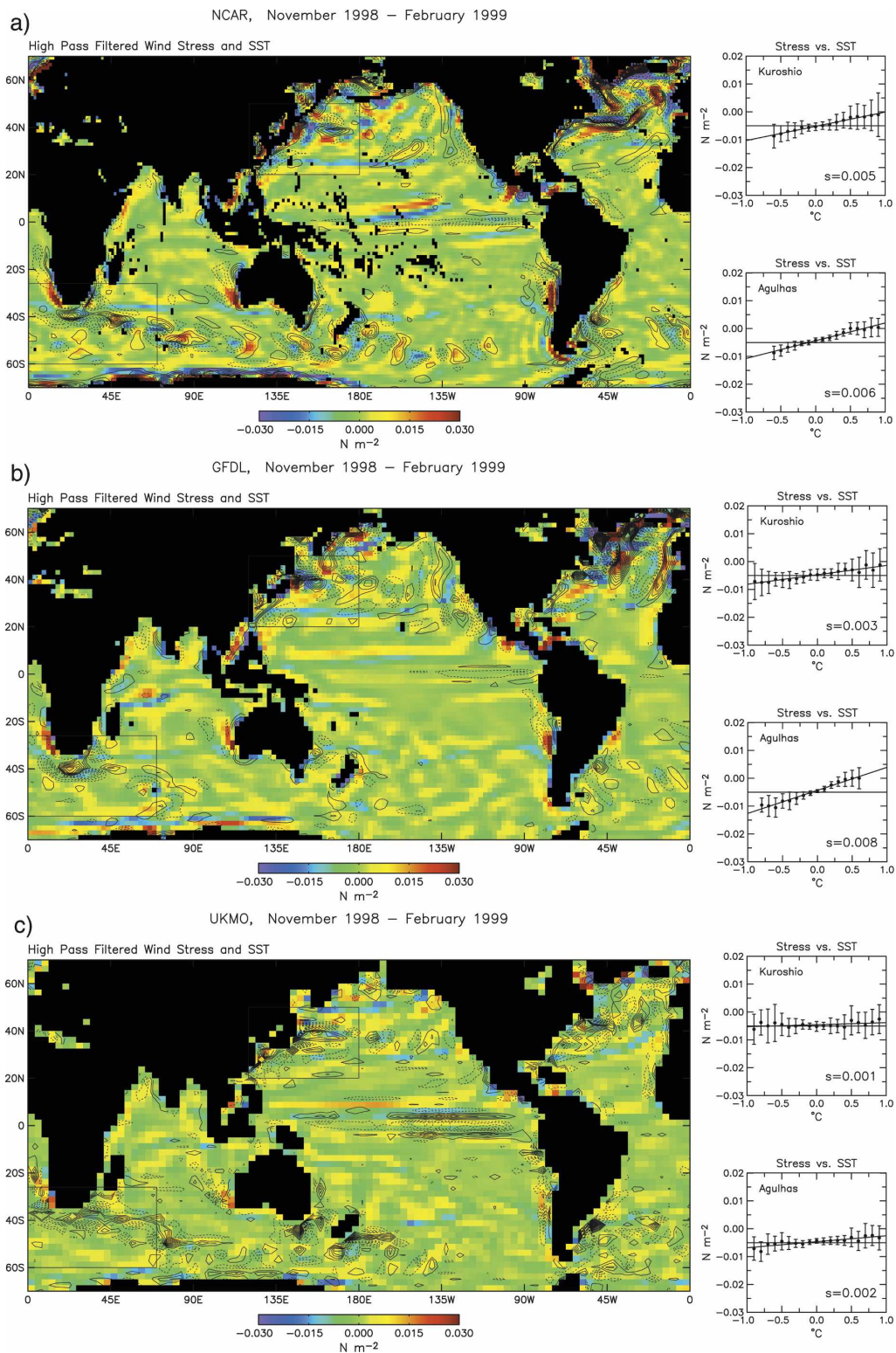


FIG. 8. Spatially high-pass-filtered wind stress (colors) and SST (contours), averaged over the interval of November 1998–February 1999 from the (a) NCAR, (b) GFDL, (c) Met Office, (d) GISS, (e) high-resolution MIROC, and (f) medium-resolution MIROC models. Contour interval is  $0.25^{\circ}C$ , with the zero contour omitted. A  $10^{\circ}$  latitude  $\times$   $30^{\circ}$  longitude loess spatial high-pass filter was applied to the fields. To the right of each map are the corresponding model binned scatterplots of SST and wind stress for the Kuroshio and Agulhas regions, as in Fig. 4.

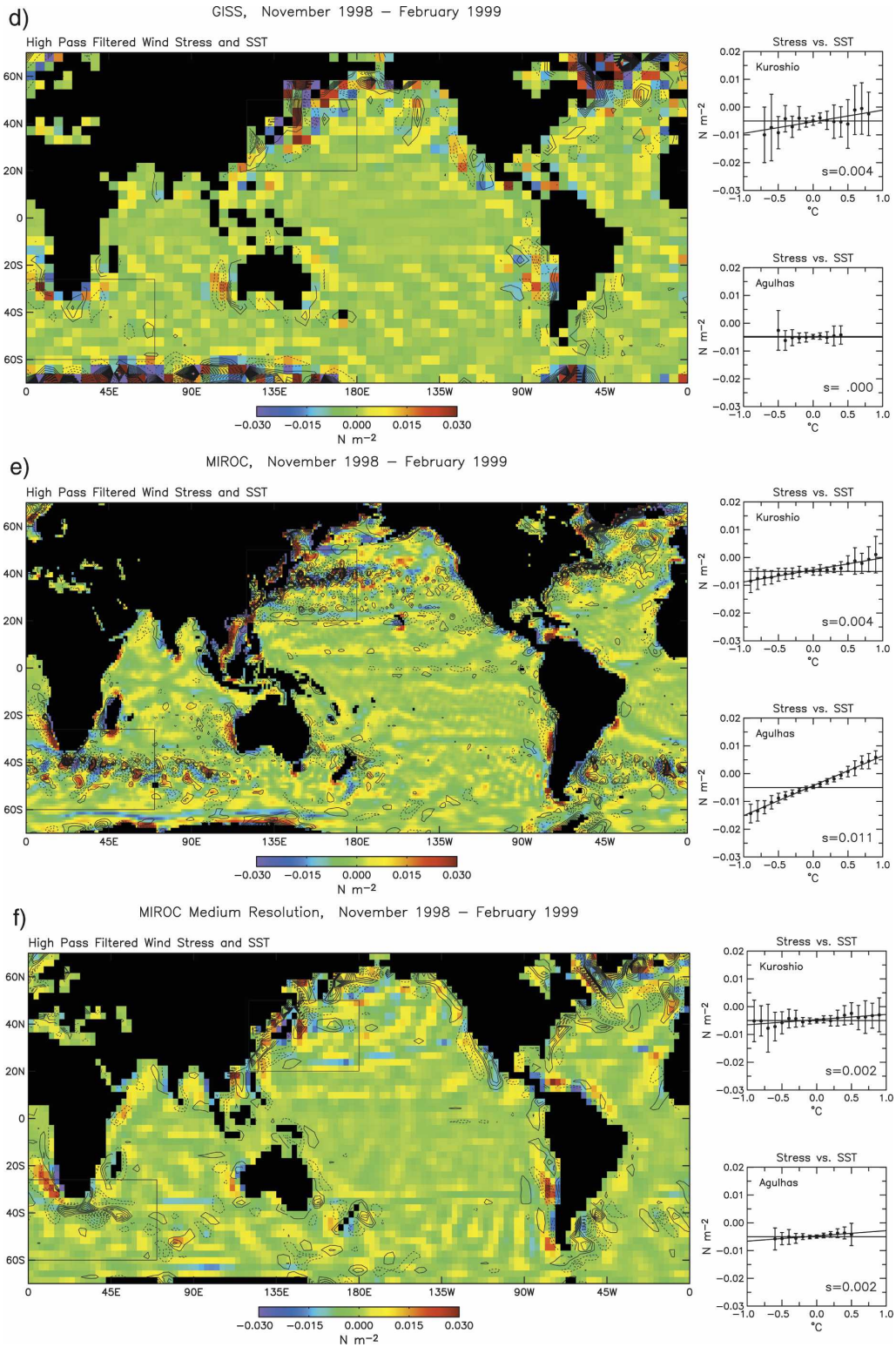


FIG. 8. (Continued)

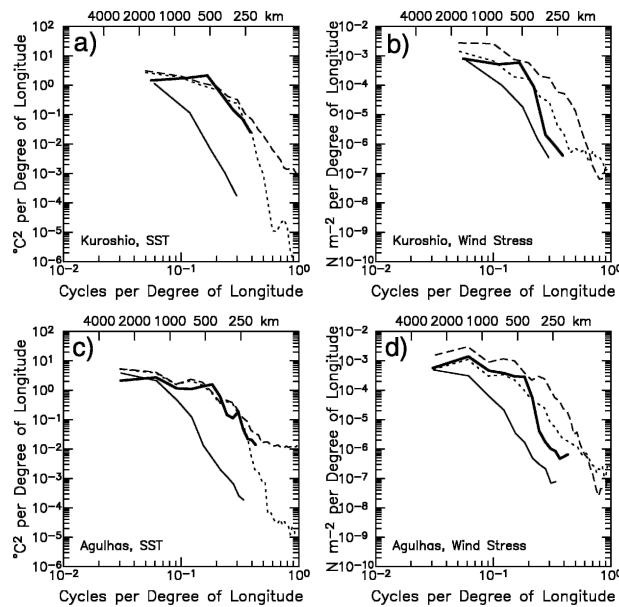


FIG. 9. Zonal wavenumber spectral density of Kuroshio region (a) SST fields from AMSR (dashed), NOAA RTG (dotted), high-resolution MIROC (boldface solid), and the NCAR model (thin solid), and (b) wind stress fields from QuikSCAT (dashed), the ECMWF operational forecast model (dotted), high-resolution MIROC (boldface solid), and the NCAR model (thin solid). (c) and (d) Same as (a) and (b), respectively, but for the Agulhas region. The wavenumber is expressed in terms of degrees of longitude on the abscissas. Corresponding wavelengths at the center latitude of each rectangular region are labeled along the top axes. The Kuroshio and Agulhas regions are defined by the boxes shown in Fig. 1a.

(Fig. 6). The relative strength of coupling compared to the ECMWF appears to be somewhat region dependent.

It is noteworthy that even the higher-resolution models exhibit regional biases associated with the spatially high-pass-filtered SST and wind stress fields. For example, note the collocation of elevated wind stress with the unrealistic “banana shaped” region of warm SST in the subtropical North Pacific in the NCAR model (Fig. 8a). This northeastward intrusion of warm water along a line running roughly between the Hawaiian Islands and the northwestern United States is particularly notable when compared with the AMSR observations in unfiltered SST fields (not shown here). The lack of response of the wind stress curl (Fig. 10b) to the strong crosswind SST gradients near 25°N may occur because this SST feature coincides with the transition between the model easterlies and westerlies where the wind stress magnitudes are weak.

Another important consideration is that, while the NCAR model and high-resolution MIROC both exhibit midlatitude air–sea coupling that is more realistic than that simulated by the other climate models con-

sidered here, both models contain spectral dynamical cores that exhibit “ringing” to the west of major mountain ranges. These biases are most notable in the wind stress divergence field in the South Pacific near the coast of South America between the latitudes of 35° and 60°S (Figs. 10a and 10c). This ringing, which is presumably caused by the influence of poorly resolved topography on the spherical harmonic truncation of the atmospheric model, does not exist in the SST field because the MIROC and NCAR ocean model use a rectangular grid.

## 5. Conclusions

The ability of six IPCC AR4 climate models to capture the observed strong relationship between SST and surface wind stress in the vicinity of strong SST fronts was investigated. The analysis emphasizes air–sea interactions associated with ocean meanders in major mid-latitude western boundary current systems such as the Agulhas Current, Kuroshio, and Gulf Stream. Such air–sea interactions have been well documented in the literature (e.g., O’Neill et al. 2003, 2005; Nonaka and Xie 2003; Xie 2004; Chelton et al., 2004). As a baseline for comparison with the climate models, we first analyzed behavior from satellite observations (section 3). Surface stress from the SeaWinds scatterometer on QuikSCAT and SST from the AMSR on EOS *Aqua* clearly indicate the influence of SST on surface wind stress on scales smaller than about 10° latitude  $\times$  30° longitude. Binned scatterplots over the Kuroshio and Agulhas Current regions show that spatially high-pass-filtered SST and wind stress variations are linearly related, with higher SST associated with higher wind stress. A similar robust linear relationship exists between wind stress divergence and the downwind SST gradient, and between wind stress curl and the crosswind SST gradient.

Although the coupling coefficients between wind stress and SST are only half as large as from satellite observations, the influence of SST on wind stress is also clearly identifiable in the ECMWF operational forecast model, which consists of a high-resolution T511 spectral core (0.35° latitude  $\times$  0.35° longitude). The specification of the SST boundary condition is crucially important to the ability of the ECMWF model to simulate realistic air–sea interactions. The SST boundary condition in the ECMWF model was changed from Reynolds SST to the higher-resolution NOAA RTG SST in May 2001, accompanied by a marked improvement in the representation of small-scale air–sea interactions near strong SST fronts.

The ability to simulate realistic air–sea interactions is present to varying degrees in the six coupled climate

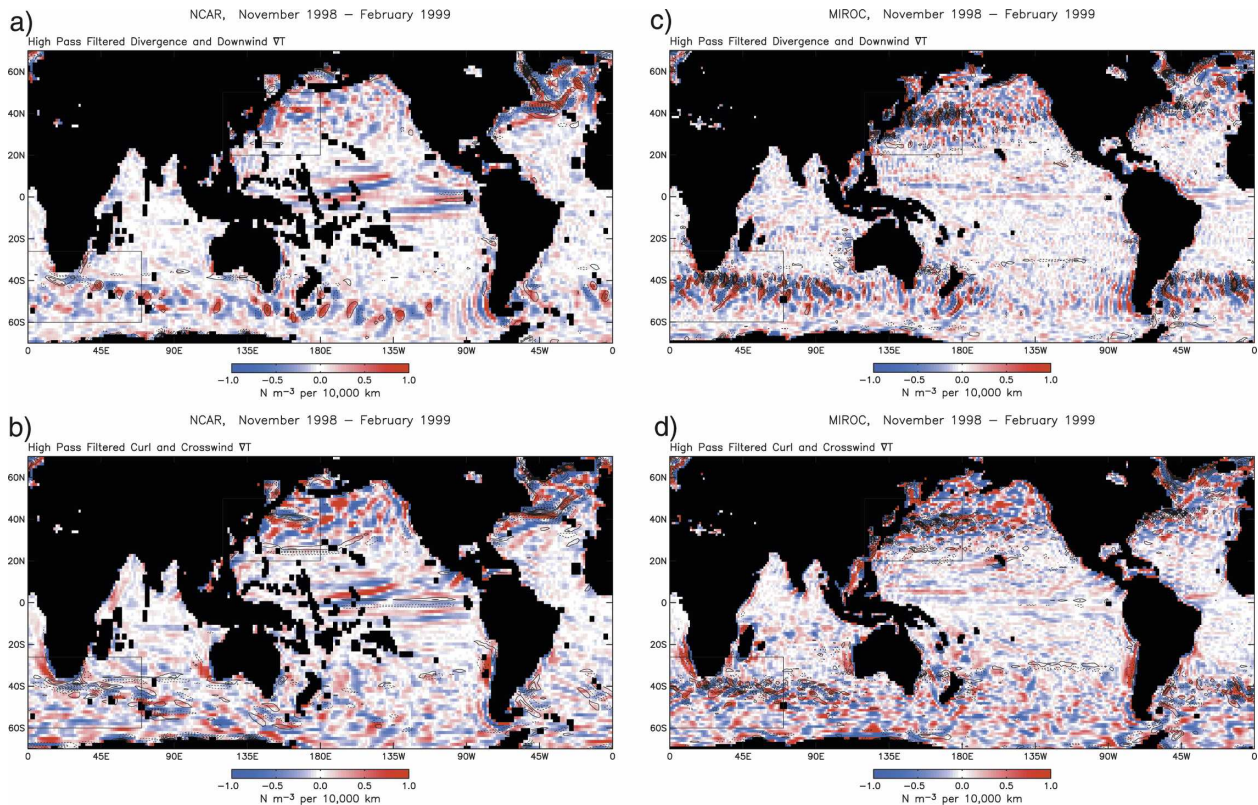


FIG. 10. Spatially high-pass-filtered wind stress divergence (colors) and downwind SST gradient (contours) from the (a) NCAR model and (c) high-resolution MIROC and wind stress curl (colors) and crosswind SST gradient (contours) from the (b) NCAR model and (d) high-resolution MIROC, averaged over the interval of November 1998–February 1999. SST gradient contour interval is  $0.25^{\circ}\text{C} (100 \text{ km})^{-1}$ , with the zero contour omitted. A  $10^{\circ}$  latitude  $\times$   $30^{\circ}$  longitude loess spatial high-pass filter was applied to the fields.

models considered here. The MIROC3.2\_HIRES and NCAR CCSM3.0 produce the most realistic air–sea coupling associated with midlatitude current systems. These models are also the highest-resolution climate models we analyzed, with the NCAR model having a grid resolution of  $1.4^{\circ} \times 1.4^{\circ}$  (T85), and MIROC3.2\_HIRES having a grid resolution of  $1.1^{\circ} \times 1.1^{\circ}$  (T106). Coupling coefficients between SST and wind stress (and between derivative wind stress and SST gradient component fields) in these two models are comparable to those in the ECMWF operational model, although they are about a factor of 2 weaker than those in the satellite observations. The spatial scales of midlatitude SST features and SST-induced wind perturbations in MIROC3.2\_HIRES are comparable to satellite observations of AMSR SST and QuikSCAT wind stress. In comparison, the spatial scales of midlatitude SST features and SST-induced wind perturbations in the NCAR model are considerably larger than observed. This may be due in part to the bathymetry in the ocean components of the coupled models. Seafloor topography is much better resolved in MIROC3.2\_HIRES than

in the NCAR model, possibly contributing to the difference in the scales of SST perturbations between the two models because the paths of ocean currents that are responsible for the small-scale variability in SST are strongly influenced by bathymetry.

Another factor limiting the realism of MIROC and the NCAR model is because the atmospheric components of these models both have spectral dynamical cores, they exhibit prominent spectral ringing signatures in the Southern Ocean to the west of the Andes. This ringing is particularly apparent in the surface wind stress divergence and is not associated with a corresponding SST signature because the ocean components of these models have rectangular grids.

The ability of climate models to simulate the air–sea interactions of interest to this study generally degrades with decreasing model grid resolution. Of particular interest is the medium-resolution MIROC ( $2.8^{\circ} \times 2.8^{\circ}$ , T42), which exhibits much weaker coupling between wind stress and SST than the higher-resolution version of the same model. The medium-resolution MIROC also has decreased vertical resolution, which may sig-

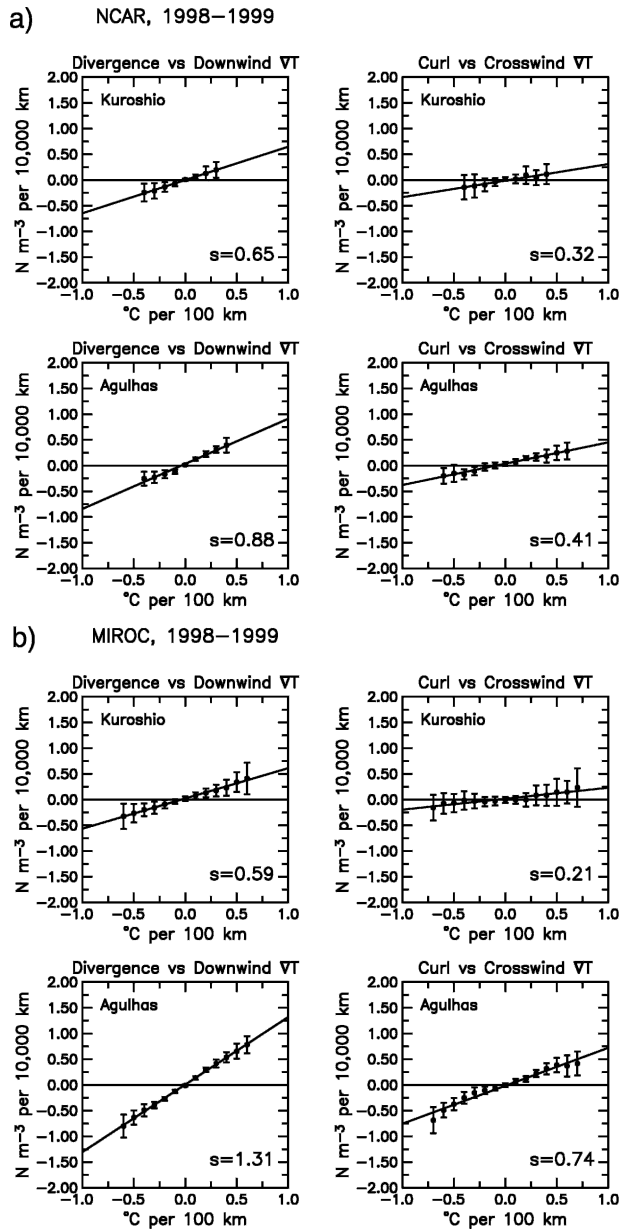


FIG. 11. Binned scatterplots showing spatially high-pass-filtered wind stress divergence binned by value of downwind SST gradient, and wind stress curl binned by value of crosswind SST gradient. Plots are shown for the Kuroshio and Agulhas regions for the (a) NCAR model and (b) high-resolution MIROC. Details of the analysis technique are described in the text.

nificantly impact the strength of coupling between SST and wind stress. The GFDL CM2.0 ( $2.0^\circ \times 2.5^\circ$ ) and Met Office HadCM3 ( $2.5^\circ \times 3.8^\circ$ ) exhibit linear relationships between SST and wind stress, as observed, although the coupling coefficients for the Met Office model are significantly weaker than for the GFDL and higher-resolution models. SST anomalies in both the

GFDL and Met Office models are more geographically confined, and the spatial scales of SST anomalies are larger than in the higher-resolution models and observations. Because of its coarse  $4^\circ \times 5^\circ$  resolution, the GISS Model ER is not able to resolve the midlatitude ocean eddies that lead to prominent air–sea interaction.

Factors that appear to limit the accuracy of the model representations of air–sea interaction associated with strong midlatitude SST fronts include atmosphere model grid resolution, the vertical resolution of the atmosphere model, and the resolution and accuracy of the SST boundary forcing used by the model. All of the climate models analyzed here have an ocean component of equal or higher horizontal grid resolution than the corresponding atmosphere model. The climate model air–sea coupling deficiencies may therefore be partially ameliorated by increasing the grid resolution of the atmosphere component models. The ECMWF operational forecast model exhibits SST–wind stress coupling that is shown to be highly dependent on the horizontal resolution of the SST boundary condition, also suggesting the importance of adequate ocean resolution for simulating realistic air–sea interactions. Deficiencies in the parameterization of boundary layer physics likely also contribute to some of the differences between models and observations.

The dynamical significance of SST-induced perturbations of the surface wind stress field is under investigation. Because these features are order-one perturbations of the background large-scale wind fields, they likely have strong feedback effects on the ocean. The wind stress perturbations will significantly modulate wind mixing of the ocean. Likewise, the persistence and intensity of Ekman upwelling associated with the wind stress curl perturbations likely have strong local feedback effects on the ocean. In addition, neglect of small-scale variability in the wind stress field can result in underestimates of the volume transports of subtropical western boundary currents by more than 20% (Milliff et al. 2004). Air–sea coupling on small spatial scales may also have significant effects on the large-scale midlatitude atmospheric flow. For example, Ciasto and Thompson (2004) find that small-spatial-scale SST anomalies in the Gulf Stream extension region precede changes in the large-scale Northern Hemisphere flow by 2 weeks. The ability of coupled climate models to properly represent air–sea coupling associated with major current systems may thus have significant implications for realistic simulation of the atmosphere–ocean climate system.

The relationship between midlatitude SST and wind stress on small spatial scales is different from the relationship commonly observed on the basin scale, where

midlatitude ocean–atmosphere interactions are characterized by a negative correlation between surface wind speed and sea surface temperature (e.g., Kushnir et al. 2002). Basin-scale atmospheric wind perturbations are perceived to regulate ocean mixed layer heat content locally through wind-driven turbulent fluxes of moist static energy and momentum. Given the positive correlation between wind stress and SST demonstrated here from satellite observations, the ECMWF forecast model, and climate models, a complete picture of midlatitude air–sea interactions should include the modification of the atmospheric flow by SST anomalies on small spatial scales.

*Acknowledgments.* We thank Michael Schlax for data processing support and for numerous suggestions during the course of this study. We also thank Michael Alexander and one anonymous reviewer for their constructive reviews of the manuscript. This research was funded by NSF and DOE as a Climate Model Evaluation Project Grant NSF ATM 0444564, under the U.S. CLIVAR Program (information available online at <http://www.usclivar.org/index.html>). Additional support for publication costs was provided by the Climate Dynamics Program of the National Science Foundation under Grant ATM-0327460. DBC was supported by NASA Grant NAS5-32965. Any opinions, findings, conclusions or recommendations expressed in this paper are those of the authors and do not necessarily reflect the views of the sponsors. We acknowledge the international modeling groups for providing their data for analysis, the Program for Climate Model Diagnosis and Intercomparison for collecting and archiving the model data, the JSC/CLIVAR Working Group on Coupled Modelling and their Coupled Model Intercomparison Project and Climate Simulation Panel for organizing the model data analysis activity, and the IPCC WG1 TSU for technical support. The IPCC Data Archive at Lawrence Livermore National Laboratory is supported by the Office of Science, U.S. Department of Energy.

#### REFERENCES

- Barsugli, J. J., and D. S. Battisti, 1998: The basic effects of atmosphere–ocean thermal coupling on midlatitude variability. *J. Atmos. Sci.*, **55**, 477–493.
- Bjerknes, J., 1964: Atlantic air–sea interaction. *Advances in Geophysics*, Vol. 10, Academic Press, 1–82.
- Boebel, O., T. Rossby, J. Lutjeharms, W. Zenk, and C. Barron, 2003: Path and variability of the Agulhas Return Current. *Deep-Sea Res.*, **50B**, 35–56.
- Bond, N. A., 1992: Observations of planetary boundary layer structure in the eastern equatorial Pacific. *J. Climate*, **5**, 699–706.
- Chelton, D. B., 2005: The impact of SST specification on ECMWF surface wind stress fields in the eastern tropical Pacific. *J. Climate*, **18**, 530–550.
- , and M. G. Schlax, 2003: The accuracies of smoothed sea surface height fields constructed from tandem altimeter datasets. *J. Atmos. Oceanic Technol.*, **20**, 1276–1302.
- , and M. H. Freilich, 2005: Scatterometer-based assessment of 10-m wind analyses from the operational ECMWF and NCEP numerical weather prediction models. *Mon. Wea. Rev.*, **133**, 409–429.
- , and F. J. Wentz, 2005: Global high-resolution satellite observations of sea surface temperature for numerical weather prediction and climate research. *Bull. Amer. Meteor. Soc.*, **86**, 1097–1115.
- , —, C. L. Gentemann, R. A. deSzoeki, and M. G. Schlax, 2000: Microwave SST observations of transequatorial tropical instability waves. *Geophys. Res. Lett.*, **27**, 1239–1242.
- Chelton, D. B., and Coauthors, 2001: Observations of coupling between surface wind stress and sea surface temperature in the eastern tropical Pacific. *J. Climate*, **14**, 1479–1498.
- , M. G. Schlax, M. H. Freilich, and R. F. Milliff, 2004: Satellite measurements reveal persistent small-scale features in ocean winds. *Science*, **303**, 978–983.
- Ciasto, L. M., and D. W. J. Thompson, 2004: North Atlantic atmosphere–ocean interaction on intraseasonal time scales. *J. Climate*, **17**, 1617–1621.
- Cox, M. D., 1984: A primitive equation, 3 dimensional model of the ocean. GFDL Ocean Group Tech. Rep. 1, 143 pp.
- Cronin, M. F., S.-P. Xie, and H. Hashizume, 2003: Barometric pressure variations associated with eastern Pacific tropical instability waves. *J. Climate*, **16**, 3050–3057.
- Delworth, T. L., and Coauthors, 2006: GFDL's CM2 global coupled climate models. Part 1: Formulation and simulation characteristics. *J. Climate*, **19**, 643–673.
- Deser, C., and M. L. Blackmon, 1993: Surface climate variations over the North Atlantic Ocean during winter—1900–1989. *J. Climate*, **6**, 1743–1753.
- de Szoeki, S. P., C. S. Bretherton, N. A. Bond, M. F. Cronin, and B. M. Morley, 2005: EPIC 95°W observations of the eastern Pacific atmospheric boundary layer from the cold tongue to the ITCZ. *J. Atmos. Sci.*, **62**, 426–442.
- Frankignoul, C., 1985: Sea surface temperature anomalies, planetary waves, and air–sea feedback in midlatitudes. *Rev. Geophys.*, **23**, 357–390.
- Gordon, C., C. Cooper, C. A. Senior, H. T. Banks, J. M. Gregory, T. C. Johns, J. F. B. Mitchell, and R. A. Wood, 2000: Simulation of SST, sea ice extents and ocean heat transports in a version of the Hadley Centre coupled model without flux adjustments. *Climate Dyn.*, **16**, 147–168.
- Hashizume, H., S.-P. Xie, W. T. Liu, and K. Takeuchi, 2001: Local and remote atmospheric response to tropical instability waves: A global view from space. *J. Geophys. Res.*, **106**, 10 173–10 185.
- , M. Fujiwara, M. Shiotani, T. Watanabe, Y. Tanimoto, W. T. Liu, and K. Takeuchi, 2002: Direct observations of atmospheric boundary layer response to slow SST variations over the eastern equatorial Pacific. *J. Climate*, **15**, 3379–3393.
- Hasumi, H., 2000: CCSR Ocean Component Model (COCO) Version 2.1. CCSR Rep. 13, 68 pp.
- , and S. Emori, Eds., 2004: K-1 coupled GCM (MIROC) description. K-1 Tech. Rep. 1, 39 pp. [Available online at <http://www.ccsr.u-tokyo.ac.jp/kyosei/hasumi/MIROC/tech-repo.pdf>.]

- Holland, W. R., and D. B. Haidvogel, 1980: A parameter study of mixed instability of idealized ocean currents. *Dyn. Atmos. Oceans*, **4**, 185–215.
- Ikeda, M., 1981: Meanders and detached eddies of a strong eastward-flowing jet using a two-layer quasi-geostrophic model. *J. Phys. Oceanogr.*, **11**, 185–215.
- Junge, M. M., and T. W. N. Haine, 2001: Mechanisms of North Atlantic wintertime sea surface temperature anomalies. *J. Climate*, **14**, 4560–4572.
- Jury, M. R., and N. Walker, 1988: Marine boundary layer modification across the edge of the Agulhas Current. *J. Geophys. Res.*, **93**, 647–654.
- Kushnir, Y., W. A. Robinson, I. Blade, N. M. J. Hall, S. Peng, and R. Sutton, 2002: Atmospheric GCM response to extratropical SST anomalies: Synthesis and evaluation. *J. Climate*, **15**, 2233–2256.
- Legeckis, R., 1977: Long waves in the eastern equatorial Pacific Ocean: A view from a geostationary satellite. *Science*, **197**, 1179–1181.
- Lindzen, R. S., and S. Nigam, 1987: On the role of sea surface temperature gradients in forcing low-level winds and convergence in the tropics. *J. Atmos. Sci.*, **44**, 2418–2436.
- Lukusch, U., and H. von Storch, 1992: Modeling the low-frequency sea surface temperature variability in the North Pacific. *J. Climate*, **5**, 893–906.
- McGauley, M., C. Zhang, and N. A. Bond, 2004: Large-scale characteristics of the atmospheric boundary layer in the eastern Pacific cold tongue–ITCZ region. *J. Climate*, **17**, 3907–3920.
- Milliff, R. F., J. Morzel, D. B. Chelton, and M. H. Freilich, 2004: Wind stress curl and wind stress divergence biases from rain effects on QSCAT surface wind retrievals. *J. Atmos. Oceanic Technol.*, **21**, 1216–1231.
- Mizuno, K., and W. B. White, 1983: Annual and interannual variability in the Kuroshio Current system. *J. Phys. Oceanogr.*, **13**, 1847–1867.
- Nakamura, H., G. Lin, and T. Yamagata, 1997: Decadal climate variability in the North Pacific during the recent decades. *Bull. Amer. Meteor. Soc.*, **78**, 2215–2225.
- Namias, J., and D. R. Cayan, 1981: Large-scale air-sea interactions and short period climate fluctuations. *Science*, **214**, 869–876.
- Nonaka, M., and S.-P. Xie, 2003: Covariations of sea surface temperature and wind over the Kuroshio and its extension: Evidence for ocean-to-atmosphere feedback. *J. Climate*, **16**, 1404–1413.
- Numaguti, A., M. Takahashi, T. Nakajima, and A. Sumi, 1997: Description of CCSR/NIES atmospheric general circulation model. *Study on the Climate System and Mass Transport by a Climate Model, CGER's Supercomputer Monograph Report*, No. 3, Center for Global Environmental Research, National Institute for Environmental Studies, 1–48.
- O'Neill, L. W., D. B. Chelton, and S. K. Esbensen, 2003: Observations of SST-induced perturbations of the wind stress field over the Southern Ocean on seasonal timescales. *J. Climate*, **16**, 2340–2354.
- , —, —, and F. J. Wentz, 2005: High-resolution satellite measurements of the atmospheric boundary layer response to SST variations along the Agulhas Return Current. *J. Climate*, **18**, 2706–2723.
- Qiao, L., and R. H. Weisberg, 1995: Tropical instability wave kinematics: Observations from the Tropical Instability Wave Experiment. *J. Geophys. Res.*, **100**, 8677–8693.
- Raymond, D. J., and Coauthors, 2004: EPIC2001 and the coupled ocean–atmosphere system of the tropical east Pacific. *Bull. Amer. Meteor. Soc.*, **85**, 1341–1354.
- Reynolds, R. W., and T. M. Smith, 1994: Improved global sea surface temperature analyses using optimum interpolation. *J. Climate*, **7**, 929–948.
- , N. A. Rayner, T. M. Smith, D. C. Stokes, and W. Wang, 2002: An improved in situ and satellite SST analysis for climate. *J. Climate*, **15**, 1609–1625.
- Russell, G. L., J. R. Miller, and D. Rind, 1995: A coupled atmosphere–ocean model for transient climate change. *Atmos.–Ocean*, **33**, 683–730.
- Schmidt, G. A., and Coauthors, 2005: Present-day atmospheric simulations using GISS ModelE: Comparison to in situ, satellite, and reanalysis data. *J. Climate*, **19**, 153–192.
- Seager, R., Y. Kushnir, M. Visbeck, N. Naik, J. Miller, G. Krahnemann, and H. Cullen, 2000: Causes of Atlantic Ocean climate variability between 1958 and 1998. *J. Climate*, **13**, 2845–2862.
- Small, J., S.-P. Xie, and Y. Wang, 2003: Numerical Simulation of Atmospheric Response to Pacific Tropical Instability Waves. *J. Climate*, **16**, 3722–3740.
- , —, and J. Hafner, 2005a: Satellite observations of mesoscale ocean features and copropagating atmospheric surface fields in the tropical belt. *J. Geophys. Res.*, **110**, C02021, doi:10.1029/2004JC002598.
- Small, R. J., S.-P. Xie, Y. Wang, S. K. Esbensen, and D. Vickers, 2005b: Numerical simulation of boundary layer structure and cross-equatorial flow in the eastern Pacific. *J. Atmos. Sci.*, **62**, 1812–1830.
- Smith, R. D., and P. R. Gent, 2002: Reference manual for the Parallel Ocean Program (POP) ocean component of the Community Climate System Model (CCSM 2.0 and 3.0). Los Alamos National Laboratory Tech. Rep. LA-UR-02-2484.
- Sweet, W., R. Fett, J. Kerling, and P. LaViolette, 1981: Air-sea interaction effects in the lower troposphere across the north wall of the Gulf Stream. *Mon. Wea. Rev.*, **109**, 1042–1052.
- Thiébaux, J., E. Rogers, W. Wang, and B. Katz, 2003: A new high-resolution blended real-time global sea surface temperature analysis. *Bull. Amer. Meteor. Soc.*, **84**, 645–656.
- Trenberth, K. E., W. G. Large, and J. G. Olson, 1990: The mean annual cycle in global ocean wind stress. *J. Phys. Oceanogr.*, **20**, 1742–1760.
- Wallace, J. M., and Q.-R. Jiang, 1987: On the observed structure of interannual variability of the atmosphere/ocean climate system. *Atmospheric and Oceanic Variability*, H. Cattle, Ed., Royal Meteorological Society, 17–43.
- , T. P. Mitchell, and C. Deser, 1989: The influence of sea surface temperature on surface wind in the eastern equatorial Pacific: Seasonal and interannual variability. *J. Climate*, **2**, 1492–1499.
- White, W. B., and J. P. McCreary, 1976: On the formation of the Kuroshio Meander and its relationship to the large-scale ocean circulation. *Deep-Sea Res.*, **23**, 33–47.
- Xie, S.-P., 2004: Satellite observations of cool ocean–atmosphere interaction. *Bull. Amer. Meteor. Soc.*, **85**, 195–208.
- Yin, B. F., and B. A. Albrecht, 2000: Spatial variability of atmospheric boundary layer structure over the eastern equatorial Pacific. *J. Climate*, **13**, 1574–1592.